Journal of MATERIALS RESEARCH

Invited Paper
DOI:10.1557/s43578-021-00353-9

ULTRA-WIDE BANDGAP MATERIALS, DEVICES, AND SYSTEMS

FOCUS ISSUE

Experimental Hall electron mobility of bulk single crystals of transparent semiconducting oxides

Zbigniew Galazka[1,a)], Klaus Irmscher[1], Mike Pietsch[1], Steffen Ganschow[1], Detlev Schulz[1], Detlef Klimm[1], Isabelle M. Hanke[1], Thomas Schroeder[1,2], Matthias Bickermann[1,3]

[1] *Leibniz-Institut für Kristallzüchtung, Max-Born-Str. 2, 12489 Berlin, Germany*
[2] *Institut für Physik, Humboldt-Universität zu Berlin, Newtonstr. 15, 12489 Berlin, Germany*
[3] *Institut für Chemie, Technische Universität Berlin, Straße des 17. Juni 115, 10623 Berlin, Germany*
[a)] Address all correspondence to this author. e-mail: zbigniew.galazka@ikz-berlin.de

Received: 8 April 2021; accepted: 16 August 2021; published online: 30 August 2021

We provide a comparative study of basic electrical properties of bulk single crystals of transparent semiconducting oxides (TSOs) obtained directly from the melt (9 compounds) and from the gas phase (1 compound), including binary (β-Ga_2O_3, In_2O_3, ZnO, SnO_2), ternary ($ZnSnO_3$, $BaSnO_3$, $MgGa_2O_4$, $ZnGa_2O_4$), and quaternary ($Zn_{1-x}Mg_xGa_2O_4$, $InGaZnO_4$) systems. Experimental outcome, covering over 200 samples measured at room temperature, revealed n-type conductivity of all TSOs with free electron concentrations (n_e) between 5×10^{15} and 5×10^{20} cm^{-3} and Hall electron mobilities (μ_H) up to 240 cm^2 V^{-1} s^{-1}. The widest range of n_e values was achieved for β-Ga_2O_3 and In_2O_3. The most electrically conducting bulk crystals are $InGaZnO_4$ and $ZnSnO_3$ with $n_e > 10^{20}$ cm^{-3} and $\mu_H > 100$ cm^2 V^{-1} s^{-1}. The highest μ_H values > 200 cm^2 V^{-1} s^{-1} were measured for SnO_2, followed by $BaSnO_3$ and In_2O_3 single crystals. In_2O_3, ZnO, $ZnSnO_3$, and $InGaZnO_4$ crystals were always conducting, while others could be turned into electrical insulators.

Introduction

Transparent semiconducting oxides (TSOs) combine semiconducting behaviour and high transparency in the visible spectrum, in some TSOs even down to the deep ultraviolet. They define a fast-growing area in solid-state physics that is relevant for both science and technology. Some of the physical properties of this class of materials, in particular transport properties thereof, are not fully understood so far, therefore, it opens an opportunity for fundamental studies of the physical properties. On the other hand, materials for study need to be obtained and this poses technological challenges, in particular when industrial applications are in quest. The TSO materials may have different forms, like nanocrystals, thin films, whether amorphous, polycrystalline, or crystalline, ceramics, and bulk single crystals. Although important properties can be gathered from ceramics and thin films they are usually affected by the composition, possible other phases, point defects, and structural defects. Due to their high structural quality and homogeneity, bulk single crystals show physical properties that are closer to intrinsic material properties than ceramics, nanocrystals, and most thin films. Additionally, bulk single crystals serve as substrates for epitaxial growth and device fabrication.

There is a wide spectrum of applications for the TSOs, including electronics, opto-electronics, piezoelectrics, photovoltaics, radiation detection, gas sensing, catalysis, and the like, which may arise not necessarily from fundamental features of the TSOs, but also from the crystal structure and/or surface properties. More details on the applications of the TSOs can be found e.g. in numerous review articles [1–10] and text books [11–16]. For some of these applications, especially for electronics, electrical properties of the materials are crucial for device operation. In particular, ultra-wide bandgaps of some of the TSOs make them suitable for high power switching devices, while materials with a very high electrical conductivity are well suited for transparent electrodes in photovoltaics and flat panel displays. Bulk crystals may function directly as active components in some of the devices (e.g. FET transistors and Schottky barrier diodes in vertical configurations) or as passive components acting as substrates for

© The Author(s) 2021

devices fabricated thereon. In the latter case, the substrates can be used for both homoepitaxy or heteroepitaxy.

A characteristic feature of the TSOs is the strong curvature of the bottom part of the conduction band (CB) enabling low electron effective mass of about $m_e^* = 0.2 - 0.3m_0$ for low to moderately high free electron concentrations ($< 10^{20}$ cm^{-3}, where band filling effects may be neglected), where m_0 is the free electron mass, and relatively high electron mobility. On the other hand, the top part of the valence band (VB) is substantially flat resulting in high hole effective masses, which in combination with hole self-trapping phenomenon makes the holes almost immobile. Therefore, the TSOs are usually considered as effective n-type semiconductors.

In the present work, we focus on basic electrical properties of bulk TSO single crystals that we grew directly from the melt (9 compounds) and from the gas phase (1 compound). Experimental results obtained on a diversity of compounds frame a comparative study of the free electron concentrations and Hall electron mobilities of bulk TSO single crystals at room temperature (RT) that may serve as a guide for other forms of materials and different concepts of devices.

The bulk TSO single crystals discussed hereinafter are listed in Table 1, along with their basic structural properties, experimental bandgaps, and electron effective masses. The TSOs belong to different crystal systems, hence, they have different structures, and experimental bandgaps ranging between 2.7 and 4.9 eV. The bandgaps are typically direct or pseudo-direct as a result of the flatness of the VB maximum. A combination of structural, physical, and surface properties of the TSOs enables to design devices with unique functionalities.

Bulk TSO single crystals

All investigated bulk TSO single crystals were grown at the Leibniz-Institut für Kristallzüchtung, Berlin, Germany. They were grown directly from the melt except SnO_2 that was obtained from the gas phase at high temperatures, as summarized in Table 2. The common features of the TSOs are high melting points and high thermal instability at high temperatures that makes the crystal growth directly from the melt really challenging. These challenges were addressed and bulk single crystals obtained, as discussed in our numerous works referenced in Table 2. High melting points of 1700–2100 °C require iridium crucibles for melt growth and high-quality refractory insulating materials. All TSOs are thermally unstable at such high temperatures leading to a substantial decomposition during growth. The most unstable compounds are those containing Sn, Zn, and In elements. Ternary and quaternary systems proceed additionally incongruent decomposition (in terms of cations ratio). The growth of TSO single crystals directly from the melt requires therefore new scientific and technological approaches and concepts, as discussed in appended references in Table 2.

The size of obtained TSO single crystals varies depending on the compound, melting point, level of thermal instability, and the growth method. The largest bulk TSO single crystals were β-Ga_2O_3 (up to 2 inch in diameter and 4 inch in length) and ZnO (33 mm in diameter and 40 mm in length), while the smallest were $ZnSnO_3$ and $InGaZnO_4$ with the size of several mm. The structural quality of most of the discussed TSO single crystals can be found in references depicted in Table 2.

The investigated samples were prepared from as-grown, annealed, and in some cases from intentionally doped crystals. Annealing and doping aimed to modify electrical properties of as-grown or undoped crystals, respectively. Undoped crystals

TABLE 1: Investigated bulk TSO single crystals, their crystal structures, optical bandgaps measured on bulk crystals at room temperature (RT), and electron effective masses near the conduction band minimum.

Compound	Crystal system, space group	Experimental lattice parameters [Å]	Experimental optical bandgap [eV]	Electron effective mass m_e^*/m_0
β-Ga_2O_3	Monoclinic, $C2/m$	$a = 12.2290$, $b = 3.0390$ $c = 5.8035$, $\beta = 103.82°$	4.85 [10]	0.26–0.28$^{(e)}$ [17]
In_2O_3	Cubic, $Ia\bar{3}$	$a = 10.1212$ [16]	2.72 [18]	0.19–0.46$^{(e)}$ [19]
ZnO	Hexagonal, $P6_3mc$	$a = 3.253$, $c = 5.213$ [20]	3.18 [16]	0.23–0.32$^{(e)}$ [21–25]
SnO_2	Tetragonal, $P4_2mnm$	$a = 4.7374$, $c = 3.1864$ [26]	3.77 [16]	0.2–0.39$^{(e)}$ [27, 28]
$ZnSnO_3$	Trigonal, $R3c$	$a = 5.2622$, $c = 14.0026$ [29]	3.90 [30]	0.32$^{(t)}$ [31]
$BaSnO_3$	Cubic, $Pm\bar{3}m$	$a = 4.117$ [32]	2.99 [33]	0.19–0.36$^{(e)}$ [34, 35]
$MgGa_2O_4$	Cubic, $Fd\bar{3}m$	$a = 8.281$ [36]	4.90 [37]	0.28–0.31$^{(t)}$ [16]
$Zn_{1-x}Mg_xGa_2O_4$	Cubic, $Fd\bar{3}m$	–	4.75 [38]	–
$ZnGa_2O_4$	Cubic, $Fd\bar{3}m$	$a = 8.3336$ [39]	4.59 [39]	0.21–0.25$^{(t)}$ [40, 41]
$InGaZnO_4$	Trigonal, $R\bar{3}m$	$a = 3.275$, $c = 25.99$ [42]	3.54	0.25–0.26$^{(t)}$ [43]

Superscripts (e) and (t) refer to experimental (both bulk crystals and thin films) and theoretical values, respectively. Theoretical values for the electron effective masses were used when experimental ones were not available according to the author's best knowledge.

© The Author(s) 2021

TABLE 2: Growth methods along with melting points and investigated samples of bulk TSO single crystals grown from the melt (all except SnO_2) and from the gas phase (SnO_2).

Compound	Melting point [°C]	Growth method	References for bulk TSO crystal growth	Investigated samples
β-Ga_2O_3	1793*	Czochralski	[10, 16, 38, 44–50]	As-grown, annealed, doped (Si, Sn, Ge, Ce, Al, Cr, Mg, Ni, Co, Cu, Li, and combinations of some of them)
In_2O_3	1950 ± 30	LASSCGM	[16, 51–53]	As-grown, annealed
ZnO	1975	Bridgman	[54–58]	As-grown, annealed
SnO_2	> 2100	PVT	[16, 59]	As-grown, annealed
$ZnSnO_3$	1750 ± 25	VGF	[60]	As-grown
$BaSnO_3$	1855 ± 25	VGF	[16, 33]	As-grown, doped (La)
$MgGa_2O_4$	1930 ± 10	Czochralski, Bridgman, Kyropoulos-like	[16, 37, 38]	As-grown, annealed, doped (Si)
$Zn_{1-x}Mg_xGa_2O_4$	1920 ± 20	VGF	[16, 38]	As-grown, annealed
$ZnGa_2O_4$	1900 ± 20	VGF	[16, 38, 39]	As-grown, annealed, doped (Si, Zr, Y)
$InGaZnO_4$	1700 ± 30	VGF	[61]	As-grown, annealed

LASSCGM levitation-assisted self-seeding crystal growth method, *PVT* physical vapour transport, *VGF* vertical gradient freeze.

*From Ref. [62].

means crystals without any intentional doping when using good purity powders (typically 5 N or 4 N in some cases) as the starting materials. Annealing was performed in the presence of oxygen or hydrogen-containing atmospheres at temperatures up to 1200 °C and 800 °C, respectively, for 1 h to 20 h. Lower annealing temperature in the case of hydrogen-containing atmospheres was necessary to avoid reduction action of hydrogen that causes a sample damage at higher temperatures. On the other hand, the TSOs are thermodynamically stable up to 1200 °C in oxygen-containing atmospheres. Doping elements were selected for a specific compound to either enhance or compensate the electrical conductivity.

Electrical characterization

The electrical conductivity and Hall effect of the crystals were measured in van der Pauw configuration at room temperature using a Hall measurement system HMS 7504 (Lake Shore). The contacts of diameters less than 0.5 mm were prepared by rubbing a little In-Ga eutectic mixture in the corners of quadratic (or rectangular) wafer samples of typically $5 \times 5 (\text{or } 3) \times 0.5 \text{mm}^3$ in size. Ohmic behaviour of these contacts was accomplished by discharging a capacitor over each two contacts, i.e. contact forming by local alloying, since otherwise, too high contact resistances and/or non-linear current–voltage characteristics prevented reliable Hall effect measurements. Electrical set-up and sample dimensions limited resistivity measurements to values up to about 10^8 Ω cm. Therefore, samples with higher resistivity could not be measured and are indicated as electrical insulators. Electron concentration and electron mobility were calculated under the assumption of a unity Hall scattering factor.

The accuracy of these values is mainly determined by the errors introduced by electrical inhomogeneities due to unintentional doping variations and structural defects (see discussion below). Our experience with collecting the big data set presented hereinafter let us estimate the deviation from the given values to be below 20–30%.

All the investigated bulk TSO single crystals showed n-type conductivity. As listed in Table 3, some of the TSOs

TABLE 3: Electrical conductivity states at room temperature of bulk TSO single crystals grown from the melt (all except SnO_2) and from the gas phase (SnO_2).

Compound	Electrically insulating	Insulating state obtained by	Conducting (as-grown)
β-Ga_2O_3	Yes	High O_2 in the growth atmosphere and/or doping with divalent ions	Yes
In_2O_3	No	–	Yes
ZnO	No	–	Yes
SnO_2	Yes	Annealing in the presence of O_2	Yes
$ZnSnO_3$	No	–	Yes
$BaSnO_3$	Yes	High O_2 in the growth atmosphere	Yes
$MgGa_2O_4$	Yes	High O_2 in the growth atmosphere or annealing in the presence of O_2	Yes
$Zn_{1-x}Mg_xGa_2O_4$	Yes	Annealing in the presence of O_2	Yes
$ZnGa_2O_4$	Yes	Annealing in the presence of O_2	Yes
$InGaZnO_4$	No	–	Yes

© The Author(s) 2021

can be obtained as electrical insulators. This was achieved either by high oxygen partial pressure in the growth atmosphere (β-Ga_2O_3, $BaSnO_3$, $MgGa_2O_4$) and/or intentional doping (β-Ga_2O_3 doped with Mg, Ni, Co), or post growth heat treatment in the presence of oxygen at temperatures typically above 700 °C (SnO_2 and Ga-based spinels, i.e. $MgGa_2O_4$, $ZnGa_2O_4$, and $Zn_{1-x}Mg_xGa_2O_4$,). Bulk single crystals of In_2O_3, ZnO, $ZnSnO_3$, and $InGaZnO_4$ were always electrically conducting independent on annealing (although it decreased the free electron concentration less than one order of magnitude). Bulk ZnO, SnO_2, and $MgGa_2O_4$ crystals could not reach highly conducting state ($> 5 \times 10^{18}$ cm^{-3}), while bulk $ZnSnO_3$ and $InGaZnO_4$ single crystals were always highly conducting, even after annealing in the presence of oxygen.

Sources of the electrical conductivity of some of the TSOs as such have intensively been studied by numerous researchers both theoretically and experimentally. Although solid conclusions were drawn in some cases, ambiguity in other cases remain. For instance, the electrical conductivity in β-Ga_2O_3 may arises from solid impurities present in the starting material/intentional doping (Si, Sn, Ge, Zr, Hf) and hydrogen [48, 63–68]; in In_2O_3 from impurities/intentional doping (Sn, Ti, Zr), fluorine, hydrogen, and possible oxygen vacancies [69–72]; in ZnO from impurities/intentional doping (such as Al, Ga, In, Sc), Zn interstitials, hydrogen, complexes [73–76]; in SnO_2 from solid impurities/intentional doping (such as Sb, As), fluorine, hydrogen [77–80]; in $BaSnO_3$ from intentional doping (La, Y, Pr, Nd, Sb), fluorine, and hydrogen [81–84]. Here we point out that the growth of bulk TSO single crystals at very high temperatures combined with high thermal instability (decomposition) might generate structural and intrinsic point defects that influence electrical properties to some extent. As an example, at high temperatures during growth, the cation distribution for all spinels is random, but becomes inverse ($MgGa_2O_4$) or normal ($ZnGa_2O_4$) at room temperature. However, not slow enough cooling may preserve antisite defects (Ga_{Mg}, Ga_{Zn}) in such systems, giving rise to electrical conductivity at RT. Antisite defects with low formation energy in $ZnGa_2O_4$ have already been theoretically predicted [85]. Similarly, electrical conductivity in $ZnSnO_3$ (Sn_{Zn}) and $InGaZnO_4$ (Ga_{Zn}) crystals may be induced due to incongruent decomposition and evaporation, as for instance concluded from the theory for $InGaZnO_4$ [86]. In addition, impurities present even in high-purity starting materials as well as in iridium crucibles, and thermal insulation may also contribute to electrical conductivity of these materials. For that reason, we do not discuss hereinafter the sources of the electrical conductivity in these materials as it requires a separate, long-lasting study. Instead, we provide an experimental output gathered from bulk crystals grown at high temperatures.

The ranges of the free electron concentration in conducting bulk TSO single crystals are presented in Fig. 1. The widest range of the free electron concentrations, covering more than three orders of magnitude, was obtained for bulk β-Ga_2O_3 single crystals. The next one is In_2O_3 with over two, and $BaSnO_3$ with about two orders of magnitude. Bulk ZnO and $MgGa_2O_4$ crystals showed the lowest span in the free electron concentrations, below one order of magnitude. High values of the free electron concentrations $> 10^{19}$ cm^{-3} were measured for bulk $BaSnO_3$ (doped with La), as well as for $ZnSnO_3$, In_2O_3, $ZnGa_2O_4$, and $InGaZnO_4$ (all undoped) single crystals. The compounds that revealed the highest free electron concentrations $> 10^{20}$ cm^{-3} are bulk $ZnSnO_3$ and $InGaZnO_4$ single crystals. Since bulk crystal growth, in particular from the melt, proceeds near thermodynamic equilibrium, the incorporation of dopants is much more limited by solubility constraints than it is the case in thin film growth. Furthermore, during cooling down of highly doped bulk crystals from the growth (melt) temperature to room temperature precipitation of dopants may take place as long as dopant diffusion is not frozen. Precipitations may lead, in turn, to the formation of other defects, such as dislocations. In general, high doping with foreign atoms disturbs single-crystal growth and results in a deteriorated structural quality. In most cases, structural defects are electrically active and in TSOs they act as acceptors compensating intentionally introduced donors. Another issue with the growth near thermodynamic equilibrium is that in wide bandgap semiconductors, as the TSOs are, self-compensation cannot effectively be suppressed. Either the

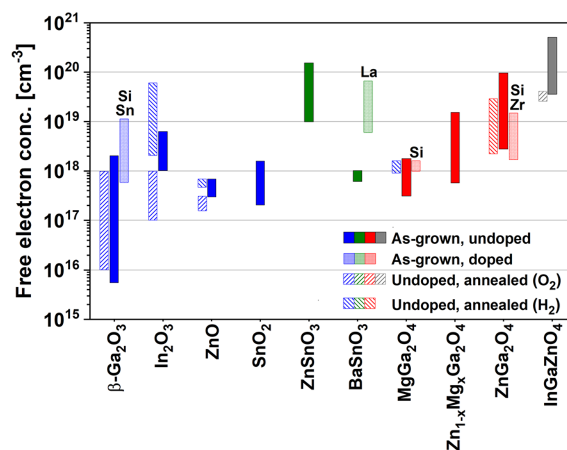

Figure 1: Range of the free electron concentrations at RT in bulk TSO single crystals grown from the melt (all except SnO_2) and from the gas phase (SnO_2). Binary systems are shown in blue, perovskites in green, Ga-based spinels in red, and the quaternary system $InGaZnO_4$ in grey. Dopants which turned to crystals into electrically insulating state or substantially had no impact on the electrical properties (β-Ga_2O_3 case) are not included. Annealing Ga-based spinels in the presence of oxygen, which turned the crystals into electrically insulating state, are not included as well. Annealed (O_2) and (H_2) refer to annealing in the presence of oxygen and hydrogen, respectively.

© The Author(s) 2021

doping atom enters different lattice sites where it acts as donor or acceptor, or its incorporation favours the formation of compensating intrinsic defects (e.g. cation vacancies). On the other hand, the free electron concentration can be higher in thin films than that in bulk crystals shown in Fig. 1. For instance, the free electron concentration in β-Ga_2O_3 films grown by metal organic vapour phase epitaxy (MOVPE) was reported at a level of 8×10^{19} cm^{-3} [87], in In_2O_3 films grown by molecular beam epitaxy (MBE) of 2×10^{21} cm^{-3} [88], in ZnO films grown by MBE of 4.1×10^{19} cm^{-3} [89], in SnO_2 films grown by MBE of 2.6×10^{20} [90], and in $BaSnO_3$ films grown by laser ablation of ~ 10^{21} cm^{-3} [91].

The essence of the present work is shown in Fig. 2 describing an experimental relation between the Hall electron mobility μ_H and free electron concentration n_e in the log–log scale. Generally, at moderate and low n_e values (< 10^{18} cm^{-3}) μ_H is limited by phonon scattering, which is defined by the compound and its crystal structure. On the other hand, at high n_e values (> 10^{18} cm^{-3}) μ_H is limited by impurity scattering. This is why one may expect a gradual decrease of μ_H with n_e if these two scattering mechanisms dominate. This relation is met by the binary systems β-Ga_2O_3, In_2O_3, ZnO, and SnO_2. It should be stressed, however, that the electron mobility is affected not only by the phonon and impurity scattering, but also by scattering on structural (dislocations, stacking faults, precipitations, grain boundaries, twins, etc.) and point (vacancies, interstitials, substitutions, complexes, impurities, etc.) defects that can be present in bulk crystals at different concentrations. This can be seen by data scattering in Fig. 2. For instance, the data scattering range of β-Ga_2O_3 and ZnO is narrow indicating high structural quality of the crystals, while it is wider for SnO_2 and In_2O_3 crystals, which indeed, often showed either low-angle grain boundaries as the result of the growth from the gas phase (SnO_2) or the formation oxygen vacancy clusters, being actually metallic In clusters, in In_2O_3 [92].

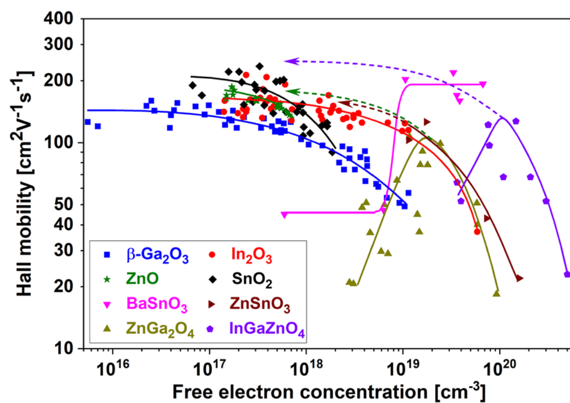

Figure 2: Log–log relation between Hall electron mobility and the free electron concentration at RT for bulk TSO single crystals grown from the melt (all except SnO_2) and from the gas phase (SnO_2). The solid lines refer to the measured values, while dashed lines to extrapolations assuming a similar trend to binary compounds (i.e. phonon scattering limitation).

Among ternary ($ZnGa_2O_4$, $MgGa_2O_4$, $BaSnO_3$, and $ZnSnO_3$) and quaternary ($Zn_{1-x}Mg_xGa_2O_4$, $InGaZnO_4$) compounds only $ZnSnO_3$ show a similar trend to binary compounds, but it is based on fewer number of measured samples having only high values of electron concentration. Other compounds within this group show a different behaviour.

A reverse $\mu_H - n_e$ relation at lower doping level of $ZnGa_2O_4$ ($n_e < 2\times10^{19}$ cm^{-3}) is likely defect related. In fact, we observed inside the crystals nanoparticles of metallic nature [39] that might form nano-Schottky contacts with the semiconducting host material resulting in charge carrier depletion zones around them with increasing extension at lower n_e leading eventually to complete blocking of current flow and apparent mobility collapse. In contrast, the depletion zones shrink with increasing n_e and allow current flow which eventually is limited by ionized impurity scattering. Both effects make a bell-like shape of the $\mu_H - n_e$ relation. Reducing or eliminating the nanoparticles in bulk $ZnGa_2O_4$ crystals may increase μ_H values to high levels (about 200 cm^2 V^{-1} s^{-1}) at low n_e values, as indicated by the dashed line in Fig. 2. Moreover, as intentional dopant concentration in $ZnGa_2O_4$ crystals is lower than the n_e concentration, that possibly arises from antisite defects [38], intentional doping might not be effective. A similar shape of the $\mu_H - n_e$ relation is also obtained for $InGaZnO_4$ in which we found inclusions of the secondary phase $In_2Ga_2ZnO_7$. The formation of this secondary phase was also pointed out during growth of $InGaZnO_4$ single crystals by the Optical Floating Zone method at a low gas pressure [93]. Also, $ZnSnO_3$ crystals contained traces of the secondary phase Zn_2SnO_4. Single crystals of $MgGa_2O_4$ (not shown in Fig. 2) showed low μ_H values of 4–7 cm^2 V^{-1} s^{-1} [38]), while $Zn_{1-x}Mg_xGa_2O_4$ (not shown in Fig. 2) an increase of μ_H with n_e in the range of 8–32 cm^2 V^{-1} s^{-1}, which is the result of an increase of Zn in favour of Mg concentrations [38]).

Bulk $BaSnO_3$ single crystals present a special case. When undoped or La-doped at low level, $n_e < 10^{19}$ cm^{-3}, μ_H values are low, about 50 cm^2 V^{-1} s^{-1}. The situation drastically changes with higher La-doping levels ($n_e > 10^{19}$ cm^{-3}), when Hall mobility jumps to high values, about or above 200 cm^2 V^{-1} s^{-1}. High electron mobility at high free electron concentrations has been explained by a physical separation of the doping sites (La^{3+} replaces Ba^{2+} in the Ba-subnetwork) and conduction channel (Sn-subnetwork) that minimizes scattering at ionized impurities, high dispersion of the bottom part of the conduction band enabling high mobility, low effective electron mass, and high dielectric constant that enhances scattering screening arising from different sources [35, 83, 102, 103]. The highest reported μ_H value for flux-grown La-doped $BaSnO_3$ single crystals is 320 cm^2 V^{-1} s^{-1} [102]. Doping the conduction channel (Sn-subnetwork) with Sb resulted, indeed, with much lower μ_H

© The Author(s) 2021

values, below 100 $cm^2\ V^{-1}\ s^{-1}$ [83]. Similar situation may be expected for other ternary and quaternary systems, in particular for $ZnSnO_3$, $ZnGa_2O_4$, and $InGaZnO_4$ single crystals when of high crystalline perfection. Indeed, these compounds revealed relatively high $\mu_H > 100\ cm^2\ V^{-1}\ s^{-1}$ at high $n_e > 10^{19}\ cm^{-3}$. We would like to stress, however, that $BaSnO_3$ crystals grown from the melt also contains nanoparticles of metallic nature that may significantly decrease the electron mobility at low doping level, in a similar way to $ZnGa_2O_4$ discussed above.

The difference in the $\mu_H - n_e$ relation between the discussed binary and ternary/quaternary systems seems to be related to a higher probability of the formation of both structural and point defects in the latter case, as discussed above. Two and three cations in the ternary and quaternary systems, respectively, increase the degree of freedom of various defect formation, which is enhanced by different partial pressures of cation-containing species leading to a fast composition shift during growth from the melt at high temperatures. Reduction of the defect density affecting the electrical properties in the ternary/quaternary systems, which is a really challenging task, would bring the $\mu_H - n_e$ relation closer to that of the binary systems with high Hall mobilities (> 150 $cm^2\ V^{-1}\ s^{-1}$) at low n_e values, as indicated by extrapolated dashed lines in Fig. 2.

Finally, Fig. 3 demonstrates a comparison of maximum μ_H (μ_{H-Max}) values of the discussed bulk TSO single crystals we measured. Out of 10 compounds, the highest μ_{H-Max} values, above 200 $cm^2\ V^{-1}\ s^{-1}$, are shown by SnO_2, $BaSnO_3$, and In_2O_3. Within a lower range of 150–200 $cm^2\ V^{-1}\ s^{-1}$ are β-Ga_2O_3 and ZnO, between 100 and 150 $cm^2\ V^{-1}\ s^{-1}$ are $ZnSnO_3$, $ZnGa_2O_4$, and $InGaZnO_4$, while below 100 $cm^2\ V^{-1}\ s^{-1}$ are Ga-based spinels containing Mg, i.e. $MgGa_2O_4$ and $Zn_{1-x}Mg_xGa_2O_4$. The record $\mu_{H-Max} = 240\ cm^2\ V^{-1}\ s^{-1}$ belongs to undoped SnO_2, also La-doped $BaSnO_3$ showed similar value of 225 $cm^2\ V^{-1}\ s^{-1}$. It seems that Sn-subnetwork in a crystal lattice enables a good electron transport with a high mobility. Undoped $ZnSnO_3$ shows lower mobility than La-doped $BaSnO_3$, but better than ed $BaSnO_3$ [33]. The transport mechanism in undoped $ZnSnO_3$ and $BaSnO_3$ crystals might be different than that of La-doped $BaSnO_3$ where the La-doping takes place at the Ba-subnetwork, while the transport through the Sn-subnetwork.

A comparison of the μ_{H-Max} values from the present study and those ever reported for the compounds discussed here along with the predicted values is summarized in Table 4. It shows that μ_{H-Max} values for bulk single crystals may reach those concluded as intrinsic limits (predicted). However, not all predicted values include all possible scattering mechanisms. Also, thin films of high structural quality and purity (here β-Ga_2O_3 and In_2O_3) resulted in higher μ_{H-Max} values as compared with bulk crystals.

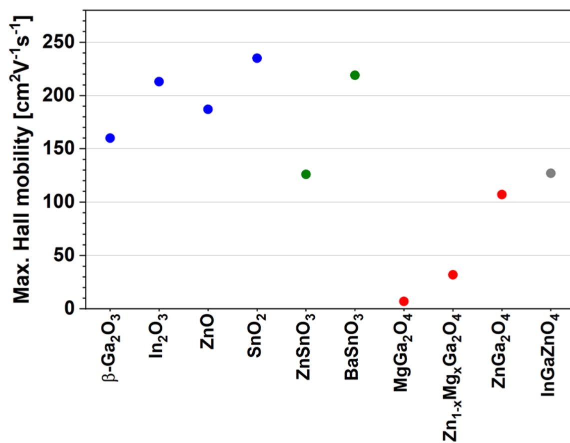

Figure 3: Maximum values of the Hall electron mobility at RT measured on bulk TSO single crystals grown from the melt (all except SnO_2) and from the gas phase (SnO_2). Binary systems are shown in blue, perovskites in green, Ga-based spinels in red, and the quaternary system $InGaZnO_4$ in grey.

TABLE 4: Maximum values of Hall electron mobility μ_{H-Max} at RT measured on bulk TSO single crystals (present work) compared with those reported in the literature and predicted.

Compound	μ_{H-Max}–present work [$cm^2\ V^{-1}\ s^{-1}$]	μ_{H-Max}–literature [$cm^2\ V^{-1}\ s^{-1}$]	μ_{H-Max}–predicted [$cm^2\ V^{-1}\ s^{-1}$]
β-Ga_2O_3	160	194 Films-MOCVD [94]	220 [95]
In_2O_3	213	226 Films-PAMBE [96]	274 [96]
ZnO	187	230 Bulk-hydrothermal [97]	233 [98]
SnO_2	240	260 Bulk-CVT [99]	265 [100]
$ZnSnO_3$	126	25 Films-sputtering [101]	–
$BaSnO_3$	225	320 Bulk-flux [102]	330 [103]
$MgGa_2O_4$	7	–	–
$Zn_{1-x}Mg_xGa_2O_4$	32	–	–
$ZnGa_2O_4$	107	20 Films-MOCVD [104]	–
$InGaZnO_4$	127	≈100 Bulk-OFZ [93]	150–200 [105]

MOCVD metal–organic chemical vapour deposition, *PAMBE* plasma-assisted molecular beam epitaxy, *CVT* chemical vapour transport.

Journal of Materials Research Volume 36 Issue 23 December 2021 www.mrs.org/jmr

© The Author(s) 2021

Summary

In the present work, we summarized basic electrical properties, i.e. free electron concentration (n_e) and Hall electron mobility (μ_H), of bulk single crystals of the TSOs, including binary (β-Ga_2O_3, In_2O_3, ZnO, SnO_2), ternary ($ZnSnO_3$, $BaSnO_3$, $MgGa_2O_4$, $ZnGa_2O_4$), and quaternary ($Zn_{1-x}Mg_xGa_2O_4$, $InGaZnO_4$) systems. Nine out of ten investigated compounds were grown directly from the melt at temperatures between 1700 and 2000 °C, and one (SnO_2) from the gas phase at the temperature of about 1600 °C.

A large data set of electrical measurements revealed n-type conductivity of all of the compounds. n_e values span for the investigated compounds between 5×10^{15} and 5×10^{20} cm^{-3} with β-Ga_2O_3 and In_2O_3 having the widest doping range, above 3 and above 2 orders of magnitude, respectively. Bulk β-Ga_2O_3, SnO_2, $BaSnO_3$, $MgGa_2O_4$, $ZnGa_2O_4$, and $Zn_{1-x}Mg_xGa_2O_4$ single crystals can be turned to electrical insulators, while others always remain at electrically conducting state independent on doping and/or annealing. The highest n_e values $> 10^{20}$ cm^{-3} were measured for bulk $InGaZnO_4$ and $ZnSnO_3$ without any intentional doping.

The highest values of $\mu_H > 200$ cm^2 V^{-1} s^{-1} were measured for SnO_2, $BaSnO_3$, and In_2O_3 single crystals. Ga-based spinels containing magnesium showed the lowest μ_H values ≤ 32 cm^2 V^{-1} s^{-1}. Some of the compounds, in particular all binary systems, well follow the $\mu_H - n_e$ relation limited by phonon scattering at lower doping range ($n_e < 10^{18}$ cm^{-3}) and by impurity scattering at higher doping range ($n_e > 10^{18}$ cm^{-3}). This relation is different, in particular for $ZnGa_2O_4$ and $InGaZnO_4$, likely due to structural defects and secondary phase traces, and for $BaSnO_3$ that depends on the doping level.

Acknowledgments

This work was partly performed in the framework of GraFOx, a Leibniz-Science Campus partially funded by the Leibniz Association—Germany. The authors express their gratitude to Dr. Andreas Popp from the Leibniz-Institut für Kristallzüchtung for critical reading of the manuscript.

Funding

Open Access funding enabled and organized by Projekt DEAL.

Data availability

Data will be made available on reasonable request.

Declarations

Conflict of interest The authors declare no conflict of interest.

Open Access

This article is licensed under a Creative Commons Attribution 4.0 International License, which permits use, sharing, adaptation, distribution and reproduction in any medium or format, as long as you give appropriate credit to the original author(s) and the source, provide a link to the Creative Commons licence, and indicate if changes were made. The images or other third party material in this article are included in the article's Creative Commons licence, unless indicated otherwise in a credit line to the material. If material is not included in the article's Creative Commons licence and your intended use is not permitted by statutory regulation or exceeds the permitted use, you will need to obtain permission directly from the copyright holder. To view a copy of this licence, visit http://creativecommons.org/licenses/by/4.0/.

References

1. H. Ohta, H. Hosono, Mater. Today **7**, 42–51 (2004)
2. Ü. Özgür, Y.I. Alivov, C. Liu, A. Teke, M.A. Reshchikov, S. Doğan, V. Avrutin, S.-J. Cho, H. Morkoç, J. Appl. Phys. **98**, 041301 (2005)
3. M. Grundmann, H. Frenzel, A. Lajn, M. Lorenz, F. Schein, H. von Wenckstern, Phys. Status Solidi A **207**, 1437–1449 (2010)
4. M. Grundmann, F. Klüpfel, R. Karsthof, P. Schlupp, F.-L. Schein, D. Splith, C. Yang, S. Bitter, H. von Wenckstern, J. Phys. D: Appl. Phys. **49**, 213001 (2016)
5. E. Fortunato, P. Barquinha, R. Martins, Adv. Mater. **24**, 2945–2986 (2012)
6. H. von Wenckstern, Adv. Electron. Mater. **3**, 1600350 (2017)
7. S. Lee, S. Jeon, R. Chaji, A. Nathan, Proc. IEEE **103**, 644–664 (2015)
8. M. Higashiwaki, H. Murakami, Y. Kumagai, A. Kuramata, Jpn. J. Appl. Phys. **55**, 1202A1 (2016)
9. S.J. Pearton, J. Yang, P.H. Cary IV., F. Ren, J. Kim, M.J. Tadjer, M.A. Mastro, Appl. Phys. Rev. **5**, 011301 (2018)
10. Z. Galazka, Semicond. Sci. Technol. **33**, 113001 (2018)
11. A.E. Delahoy, S. Guo, Transparent conducting oxides for photovoltaics, in *Handbook of Photovoltaic Science and Engineering*, 2nd edn., ed. by A. Luque, S. Hegedus (Wiley, Hoboken, 2011)
12. D.S. Ginley, H. Hosono, D.C. Paine (eds.), *Handbook of Transparent Conductors* (Springer, Boston, 2010)
13. P. Barquinha, R. Martins, L. Pereira, E. Fortunato, *Transparent Oxide Electronics: From Materials to Devices* (Wiley, Hoboken, 2012)
14. S. Pearton, F. Ren, M. Mastro (eds.), *Gallium Oxide Technology, Devices and Applications* (Elsevier, Amsterdam, 2019)
15. M. Higashiwaki, S. Fujita (eds.), *Gallium Oxide, Material Properties, Crystal Growth, and Devices* (Springer, Cham, 2020)

© The Author(s) 2021

16. Z. Galazka, *Transparent Semiconducting Oxides—Bulk Crystal Growth and Fundamental Properties* (Jenny Stanford Publishing, Dubai, 2020)
17. C. Janowitz, V. Scherer, M. Mohamed, A. Krapf, H. Dwelk, R. Manzke, Z. Galazka, R. Uecker, K. Irmscher, R. Fornari, M. Michling, D. Schmeißer, J.R. Weber, J.B. Varley, C.G. Van de Walle, New J. Phys. **13**, 085014 (2011)
18. K. Irmscher, M. Naumann, M. Pietsch, Z. Galazka, R. Uecker, T. Schulz, R. Schewski, M. Albrecht, R. Fornari, Phys. Status Solidi A **211**, 54–58 (2014)
19. M. Feneberg, J. Nixdorf, C. Lidig, R. Goldhahn, Z. Galazka, O. Bierwagen, J.S. Speck, Phys. Rev. B **93**, 045203 (2016)
20. H. Schulz, K.H. Thiemann, Solid State Commun. **32**, 783–785 (1979)
21. W.S. Baer, Phys. Rev. **154**, 785–789 (1967)
22. K.J. Button, D.R. Cohn, M. von Ortenverger, B. Lax, E. Mollwo, R. Helbig, Phys. Rev. Lett. **28**, 1637–1639 (1972)
23. R.L. Wieher, Phys. Rev. **152**, 736–739 (1966)
24. J. Tang, L.Y. Deng, C.B. Tay, X.H. Zhang, J.W. Chai, H. Qin, H.W. Liu, T. Venkatesan, S.J. Chua, J. Appl. Phys. **115**, 033111 (2014)
25. Y. Wang, J. Zhu, W. Tang, Appl. Phys. Lett. **104**, 212103 (2014)
26. A. Bolzan, C. Fong, B.J. Brendan, J. Kennedy, C.J. Howard, Acta Cryst. B **53**, 373–380 (1997)
27. M. Feneberg, C. Lidig, K. Lange, M.E. White, M.Y. Tsai, J.S. Speck, O. Bierwagen, R. Goldhahn, Phys. Status Solidi A **211**, 82–86 (2014)
28. M. Feneberg, C. Lidig, M.E. White, M.Y. Tsai, J.S. Speck, O. Bierwagen, Z. Galazka, R. Goldhahn, APL Mater. **7**, 022508 (2019)
29. Y. Inaguma, M. Yoshida, T. Katsumata, J. Am. Chem. Soc. **130**, 6704–6705 (2008)
30. M. Miyauchi, Z. Liu, Z.-G. Zhao, S. Anandan, K. Hara, Chem. Commun. **46**, 1529–1531 (2010)
31. K.P. Ong, X. Fan, A. Subedi, M.B. Sullivan, D.J. Singh, APL Mater. **3**, 062505 (2015)
32. A.J. Smith, A.J.E. Welch, Acta Crystallogr. **13**, 653–656 (1960)
33. Z. Galazka, R. Uecker, K. Irmscher, D. Klimm, R. Bertram, A. Kwasniewski, M. Naumann, R. Schewski, M. Pietsch, U. Juda, A. Fiedler, M. Albrecht, S. Ganschow, T. Markurt, C. Guguschev, M. Bickermann, J. Phys. Condens. Matter. **29**, 075701 (2017)
34. C.A. Niedermeier, S. Rhode, S. Fearn, K. Ide, M.A. Moram, H. Hiramatsu, H. Hosono, T. Kamiya, Appl. Phys. Lett. **108**, 172101 (2016)
35. C.A. Niedermeier, S. Rhode, K. Ide, H. Hiramatsu, H. Hosono, T. Kamiya, M.A. Moram, Phys. Rev. B **95**, 161202 (2017)
36. L. Schwarz, Z. Galazka, T.M. Gesing, D. Klimm, Cryst. Res. Technol. **50**, 961–966 (2015)
37. Z. Galazka, D. Klimm, K. Irmscher, R. Uecker, M. Pietsch, R. Bertram, M. Naumann, M. Albrecht, A. Kwasniewski, R. Schewski, M. Bickermann, Phys. Status Solidi A **212**, 1455–1460 (2015)
38. Z. Galazka, S. Ganschow, K. Irmscher, D. Klimm, M. Albrecht, R. Schewski, M. Pietsch, T. Schulz, A. Dittmar, A. Kwasniewski, R. Grueneberg, S. Bin Anooz, A. Popp, U. Juda, I.M. Hanke, T. Schroeder, M. Bickermann, Prog. Cryst. Growth Charact. Mater. **67**, 100511 (2021)
39. Z. Galazka, S. Ganschow, R. Schewski, K. Irmscher, D. Klimm, A. Kwasniewski, M. Pietsch, A. Fiedler, I. Schulze-Jonack, M. Albrecht, T. Schröder, M. Bickermann, APL Mater. **7**, 022512 (2019)
40. S.K. Sampath, D.G. Kanhere, R. Pandey, J. Phys. Condens. Matter. **11**, 3635–3644 (1999)
41. H. Dixit, N. Tandon, S. Cottenier, R. Saniz, D. Lamoen, B. Partoens, V. Van Speybroeck, M. Waroquier, New J. Phys. **13**, 063002 (2011)
42. W. Assenmacher, G. Schnakenburg, Y. Michiue, Y. Kanke, N. Kimizuka, W. Mader, J. Solid State Chem. **215**, 176–183 (2014)
43. K. Iordanidou, C. Persson, Mater. Sci. Semicond. Process. **121**, 105297 (2021)
44. Z. Galazka, R. Uecker, K. Irmscher, M. Albrecht, D. Klimm, M. Pietsch, M. Brützam, R. Bertram, S. Ganschow, R. Fornari, Cryst. Res. Technol. **45**, 1229–1236 (2010)
45. Z. Galazka, K. Irmscher, R. Uecker, R. Bertram, M. Pietsch, A. Kwasniewski, M. Naumann, T. Schulz, R. Schewski, D. Klimm, M. Bickermann, J. Cryst. Growth **404**, 184–191 (2014)
46. Z. Galazka, R. Uecker, D. Klimm, K. Irmscher, M. Naumann, M. Pietsch, A. Kwasniewski, R. Bertram, S. Ganschow, M. Bickermann, ECS J. Solid State Sci. Technol. **6**, Q3007–Q3011 (2017)
47. Z. Galazka, S. Ganschow, A. Fiedler, R. Bertram, D. Klimm, K. Irmscher, R. Schewski, M. Pietsch, M. Albrecht, M. Bickermann, J. Cryst. Growth **486**, 82–90 (2018)
48. Z. Galazka, K. Irmscher, R. Schewski, I.M. Hanke, M. Pietsch, S. Ganschow, D. Klimm, A. Dittmar, A. Fiedler, T. Schroeder, M. Bickermann, J. Cryst. Growth **529**, 125297 (2020)
49. Z. Galazka, R. Schewski, K. Irmscher, W. Drozdowski, M.E. Witkowski, M. Makowski, A.J. Wojtowicz, I.M. Hanke, M. Pietsch, T. Schulz, D. Klimm, S. Ganschow, A. Dittmar, A. Fiedler, T. Schroeder, M. Bickermann, J. Alloy. Compd. **818**, 152842 (2020)
50. Z. Galazka, Czochralski method, in *Gallium Oxide: Crystal Growth, Materials Properties, and Devices*. ed. by M. Higashiwaki, S. Fujita (Springer, Cham, 2020), pp. 15–36
51. Z. Galazka, R. Uecker, K. Irmscher, D. Schulz, D. Klimm, M. Albrecht, M. Pietsch, S. Ganschow, A. Kwasniewski, R. Fornari, J. Cryst. Growth **362**, 349–352 (2013)
52. Z. Galazka, R. Uecker, R. Fornari, J. Cryst. Growth **388**, 61–69 (2014)
53. Z. Galazka, K. Irmscher, M. Pietsch, T. Schulz, R. Uecker, D. Klimm, R. Fornari, CrystEngComm **15**, 2220–2226 (2013)

© The Author(s) 2021

54. D. Schulz, S. Ganschow, D. Klimm, M. Neubert, M. Rossberg, M. Schmidbauer, R. Fornari, J. Cryst. Growth **296**, 27–30 (2006)
55. D. Schulz, S. Ganschow, D. Klimm, K. Struve, J. Cryst. Growth **310**, 1832–1835 (2008)
56. D. Klimm, S. Ganschow, D. Schulz, R. Fornari, J. Cryst. Growth **310**, 3009–3013 (2008)
57. D. Schulz, S. Ganschow, D. Klimm, Mater. Res. Soc. Symp. Proc. **1201**, 120-H06-10 (2010)
58. K. Jacobs, D. Schulz, D. Klimm, S. Ganschow, Solid State Sci. **12**, 307–310 (2010)
59. Z. Galazka, R. Uecker, D. Klimm, K. Irmscher, M. Pietsch, R. Schewski, M. Albrecht, A. Kwasniewski, S. Ganschow, D. Schulz, C. Guguschev, R. Bertram, M. Bickermann, R. Fornari, Phys. Status Solidi A **211**, 66–73 (2014)
60. Z. Galazka, I.M. Hanke; Leibniz-Institut für Kristallzüchtung, Berlin, Germany (2019), unpublished data.
61. Z. Galazka, I.M. Hanke; Leibniz-Institut für Kristallzüchtung, Berlin, Germany (2016), unpublished data.
62. K. Hoshikawa, E. Ohba, T. Kobayashi, J. Yanagisawa, C. Miyagawa, Y. Nakamura, J. Cryst. Growth **447**, 36–41 (2016)
63. E.G. Villora, K. Shimamura, Y. Yoshikawa, T. Ujiie, K. Aoki, Appl. Phys. Lett. **92**, 202120 (2008)
64. J.B. Varley, H. Peelaers, A. Janotti, C.G. Van de Walle, J. Phys.: Condens. Matter **23**, 334212 (2011)
65. A. Kuramata, K. Koshi, S. Watanabe, Y. Yamaoka, T. Masui, S. Yamakoshi, Jpn. J. Appl. Phys. **55**, 1202A2 (2016)
66. E. Ahmadi, O.S. Koksaldi, S.W. Kaun, Y. Oshima, D.B. Short, U.K. Mishra, J.S. Speck, Appl. Phys. Express **10**, 041102 (2017)
67. M. Saleh, A. Bhattacharyya, J.B. Varley, S. Swain, J. Jesenovec, S. Krishnamoorthy, K. Lynn, Appl. Phys. Express **12**, 085502 (2019)
68. M. Saleh, J.B. Varley, J. Jesenovec, A. Bhattacharyya, S. Krishnamoorthy, S. Swain, K. Lynn, Semicond. Sci. Technol. **35**, 04LT01 (2020)
69. O. Bierwagen, Semicond. Sci. Technol. **30**, 024001 (2015)
70. S. Limpijumnong, P. Reunchan, A. Janotti, C.G. Van de Walle, Phys. Rev. B **80**, 193202 (2009)
71. J.B. Varley, H. Peelaers, A. Janotti, C.G. Van de Walle, J. Phys. Condens. Matter **23**, 334212 (2011)
72. P. Ágoston, P. Erhart, A. Klein, K. Albe, J. Phys. Condens. Matter **21**, 455801 (2009)
73. R. Helbig, J. Cryst. Growth **15**, 25–31 (1972)
74. C.G. Van de Walle, Phys. Rev. Lett. **85**, 1012–1015 (2000)
75. E.V. Lavrov, F. Herklotz, J. Weber, Phys. Rev. B **79**, 165210 (2009)
76. D.C. Look, J.W. Hemsky, J.R. Sizelove, Phys. Rev. Lett. **82**, 2552–2555 (1999)
77. J.B. Varley, A. Janotti, C.G. Van de Walle, Phys. Rev. B **81**, 245216 (2010)
78. Z. Remes, M. Vanecek, H.M. Yates, P. Evans, D.W. Sheel, Thin Solid Films **517**, 6287–6289 (2009)
79. D.O. Scanlon, G.W. Watson, J. Mater. Chem. **22**, 25236 (2012)
80. P.D.C. King, R.L. Lichti, Y.G. Celebi, J.M. Gil, R.C. Vilão, H.V. Alberto, J.P. Duarte, D.J. Payne, R.G. Egdell, I. McKenzie, C.F. McConville, S.F.J. Cox, T.D. Veal, Phys. Rev. B **80**, 081201 (2009)
81. X. Luo, Y.S. Oh, A. Sirenko, P. Gao, T.A. Tyson, K. Char, S.-W. Cheong, Appl. Phys. Lett. **100**, 172112 (2012)
82. E. McCalla, D. Phelan, M.J. Krogstad, B. Dabrowski, C. Leighton, Phys. Rev. Meter. **2**, 084601 (2018)
83. H.J. Kim, J. Kim, T.H. Kim, W.-J. Lee, B.-G. Jeon, J.-Y. Park, W.S. Choi, D.W. Jeong, S.H. Lee, J. Yu, T.W. Noh, K.H. Kim, Phys. Rev. B **88**, 125204 (2013)
84. D.O. Scanlon, Phys. Rev. B **87**, 161201 (2013)
85. S.C. Badescu, M.D. Santia, D.C. Look, K.D. Leedy; contribution at SPIE Photonic West, February 2020, San Francisco, entitled "*First-principles modelling of native point defects in zinc gallate*"
86. A. Murat, A.U. Adler, T.O. Mason, J.E. Medvedeva, J. Am. Chem. Soc. **135**, 5685–5692 (2013)
87. M. Baldini, M. Albrecht, A. Fiedler, K. Irmscher, R. Schewski, G. Wagner, ECS J. Solid State Sci. Technol. **6**, Q3040–Q3044 (2017)
88. O. Bierwagen, J.S. Speck, Phys. Status Solidi A **211**, 48–53 (2014)
89. H. Tampo, H. Shibata, P. Fons, A. Yamada, K. Matsubara, K. Iwata, K. Tamura, H. Takasu, S. Niki, J. Cryst. Growth **278**, 268–272 (2005)
90. M.E. White, O. Bierwagen, M.Y. Tsai, J.S. Speck, J. Appl. Phys. **106**, 093704 (2009)
91. H.F. Wang, Q.Z. Liu, F. Chen, G.Y. Gao, W. Wu, X.H. Chen, J. Appl. Phys. **101**, 106105 (2007)
92. M. Albrecht, R. Schewski, K. Irmscher, Z. Galazka, T. Markurt, M. Naumann, T. Schulz, R. Uecker, R. Fornari, S. Meuret, M. Kociak, J. Appl. Phys. **115**, 053504 (2014)
93. Y. Tanaka, K. Wada, Y. Kobayashi, T. Fujii, S.J. Denholme, R. Sekine, N. Kase, N. Kimizuka, N. Miyakawa, CrystEngComm **21**, 2985–2993 (2019)
94. Z. Feng, A.F.M.A.U. Bhuiyan, Z. Xia, W. Moore, Z. Chen, J.F. McGlone, D.R. Daughton, A.R. Arehart, S.A. Ringel, S. Rajan, H. Zhao, Phys. Status Solidi RRL **14**, 2000145 (2020)
95. N. Ma, N. Tanen, A. Verma, Z. Guo, T. Luo, H. (Grace) Xing, D. Jena, Appl. Phys. Lett. **109**, 212101 (2016)
96. O. Bierwagen, J.S. Speck, Appl. Phys. Lett. **97**, 072103 (2010)
97. M.W. Allen, P. Miller, R.J. Reeves, S.M. Durbin, Appl. Phys. Lett. **90**, 062104 (2007)
98. X. Yang, C. Xu, N.C. Giles, J. Appl. Phys. **104**, 073727 (2008)
99. C.G. Fonstad, R.H. Rediker, J. Appl. Phys. **42**, 2911–2918 (1971)
100. Y. Hu, J. Hwang, Y. Lee, P. Conlin, D.G. Schlom, S. Datta, K. Cho, J. Appl. Phys. **126**, 185701 (2019)
101. F.-Y. Wu, J.-W. Li, Y. Qi, W.-T. Ding, Y.-Y. Guo, Y.-W. Zhou, Acta Metall. Sin. **29**, 827–833 (2016)

© The Author(s) 2021

102. H.J. Kim, U. Kim, H.M. Kim, T.H. Kim, H.S. Mun, B.-G. Jeon, K.T. Hong, W.-J. Lee, C. Ju, K.H. Kim, K. Char, Appl. Phys. Express **5**, 061102 (2012)
103. K. Krishnaswamy, B. Himmetoglu, Y. Kang, A. Janotti, C.G. Van de Walle, Phys. Rev. B **95**, 205202 (2017)
104. D.C. Look, K.D. Leedy, R.-H. Horng, M.D. Santia, S.C. Badescu, Appl. Phys. Lett. **116**, 252104 (2020)
105. Y. Jegal, A.H. Kulahlioglu, C.-K. Baek, B.D. Kong, IEEE Electron. Device Lett. **41**, 872–875 (2020)

© The Author(s) 2021